found that quite large reflections are induced by the RVS model if the actual physical impedance is used to assign the constant value of R_s into the RVS region. Numerical results indicate that, to reduce the reflections caused by the RVS model, the effective impedance (instead of the actual physical impedance) of the strip lines should be used. Consequently, it can be anticipated that, to improve the accuracy of the numerical results, a similar procedure (i.e., like the way to find the effective impedance for the RVS model proposed in this paper) should be adopted when other lumped elements (e.g., a capacitor or an inductor) are employed for the modeling of either passive or active microstrip devices.

REFERENCES

1. T. Shibata and H. Kimura, Computer-aided engineering for microwave and millimeter-wave circuits using the FD-TD technique of field simulations, Int J Microwave Millimeter-Wave Computer-Aided Eng 3 (1993), 238–249.
2. O.P.M. Pekonen, J. Xu, and K.I. Nikoskinen, Rigorous analysis of circuit parameter extraction from an FDTD simulation excited with a resistive voltage source, Microwave Opt Technol Lett 12 (1996), 205–210.
3. M. Piket-May, A. Taflove, and J. Baron, FD-TD modeling of digital signal propagation in 3-D circuits with passive and active loads, IEEE Trans Microwave Theory Tech 42 (1994), 1514–1532.
4. C.H. Durney, W. Sui, D.A. Christensen, and J. Zhu, A general formulation for connecting sources and passive lumped-circuit elements across multiple 3-D FDTD cells, IEEE Microwave Guided Wave Lett 6 (1996), 85–87.
5. D.M. Sheen, S.M. Ali, M.D. Abouzahra, and J.A. Kong, Application of the three-dimensional finite-difference time-domain method to the analysis of planar microstrip circuits, IEEE Trans Microwave Theory Tech 38 (1990), 849–857.
6. A.P. Zhao and A.V. Raisanen, Application of a simple and efficient source excitation technique to the FDTD analysis of waveguide and microstrip circuits, IEEE Trans Microwave Theory Tech 44 (1996), 1535–1539.
7. X. Zhang, J. Fang, K.K. Mei, and Y. Liu, Calculations of the dispersive characteristics of microstrips by the time-domain finite difference method, IEEE Trans Microwave Theory Tech 36 (1988), 263–267.
8. J.-P. Berenger, A perfectly matched layer for the absorption of electromagnetic waves, J Comput Phys 114 (1994), 185–200.

RADAR IMAGE STUDIES OF AN OCEAN-LIKE SURFACE

Hyunjun Kim[1] and Joel T. Johnson[1]
[1] Department of Electrical Engineering
ElectroScience Laboratory
The Ohio State University
Columbus, Ohio 43212

Received 30 March 2001

ABSTRACT: *High-resolution radar images of a 1-D ocean-like surface are formed through back-projection tomography. The surface profile is described by a Pierson–Moskowitz spectrum, and satisfies an impedance boundary condition. Backscatter results from 10 to 14 GHz excited by a tapered beam at incidence angles from 60 to 80° are considered. Radar images from approximate and numerical scattering models demonstrate dominant Bragg scattering components, small multiple interaction effects associated with the long-wave portion of the surface spectrum, and significant polarization dependencies.* © 2001 John Wiley & Sons, Inc. Microwave Opt Technol Lett 30: 381–384, 2001.

Key words: *rough surface scattering; radar imaging; back-projection tomography; small-slope approximation; multiple scattering*

1. INTRODUCTION

In recent years, several analytical models for rough-surface scattering have shown promising results for specified ranges of surface statistics [1, 2]. No approximate solutions, however, clearly explain all possible scattering mechanisms for a single-surface realization since the evaluation of analytical theories is typically based on results for an averaged cross section over surface realizations. Imaging techniques can offer a unique tool for the analysis and better understanding of rough-surface scattering phenomena. The recent development of efficient numerical methods for backscattering predictions has enabled radar image formation, and images formed from numerical scattering models can be used as a reference solution to evaluate the performance of the existing analytical models.

Preliminary studies of a single surface with a Gaussian roughness spectrum have shown that multiple-scattering effects can occur at near normal incident angles, and become more significant as the rms height increases [3]. The surface considered had correlation lengths which were relatively large compared to the observing wavelengths, so a simple ray-tracing algorithm was found successful in predicting multiple-scattering image locations. Images also revealed that multiple-scattering effects were captured successfully from the lowest order nonlocal small-slope approximation (NLSSA), especially in VV polarization. At moderate incidence angles, multiple-scattering events were no longer observable for the surfaces considered.

In this paper, high-spatial-resolution 10–14 GHz radar images of a Pierson–Moskowitz (P–M) ocean-like surface formed from backscatter data at incidence angles ranging from 60 to 80° are studied. In contrast to previous image studies, the P–M surface will illustrate scattering effects which can occur with a range of surface roughness scales, including Bragg scattering components. Images will be examined to determine if long-wave "tilting" effects predicted by a composite surface model [4] are observed.

In Section 2, the scattering geometry and numerical and approximate scattering models to be evaluated are described, followed by the 2-D synthetic aperture radar (SAR) image formation procedure. In Section 3, detailed investigations of numerical and approximate radar images are described in terms of major and secondary scattering events, polarization dependence, and surface-roughness-length scale effects.

2. SCATTERING GEOMETRY AND SCATTERING THEORIES

Figure 1 illustrates the scattering geometry of a 1-D rough surface, $z = f(x)$, described as a realization of a Gaussian random process with a Pierson–Moskowitz (P–M) spectrum. The P–M ocean-like surface has a multiscale roughness, and has a spectrum that is parameterized by the 19.5 m wind speed parameter w (in m/s) as

$$W(k) = \begin{cases} (\alpha/4|k|^3)\exp[-(\beta g^2/|k|^2 w^4)], \\ \qquad \text{if } k_{dl} \le k \le k_{du} \\ 0, \qquad \text{otherwise} \end{cases} \tag{1}$$

where k represents the spatial wavenumber of the surface, $\alpha = 0.008$, $\beta = 0.74$, and $g = 9.81$ m/s^2. Note that the high-frequency (i.e., short-wave) behavior of the surface is proportional to a $1/k^3$ power-law spectrum. The effects of varying

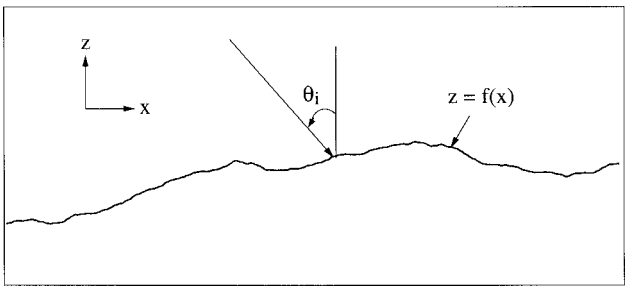

Figure 1 Scattering geometry of a rough surface

surface-length scales can be studied by passing this spectrum through a bandpass filter with high and low cutoff frequencies k_{du} and k_{dl}, as indicated in Eq. (1). The original surface profile considered in this paper is generated for a wind speed of 6 m/s and with cutoff frequencies $k_{dl} = 0.2$ rad/m (below the spectrum low-frequency "roll-off" point) and $k_{du} = 587$ rad/m (corresponding to one-half electromagnetic wavelength at 14 GHz) to ensure that all important length scales are captured. The resulting profile is 30.72 m long. However, radar images are formed only for an $L = 7.68$ m portion (ranging from 256 to 358.4 electromagnetic wavelengths) of this surface to reduce the computational requirements in image formation. The imaged surface has a height standard deviation of 10 cm, and remains very rough in terms of the electromagnetic wavelengths at these frequencies. The medium is assumed to be described by an impedance boundary condition (IBC) with a relative permittivity of $(39.7 + i40.2)$ to approximate the high-loss sea-water surface in the *Ku*-band.

Because the surface profile used is of finite size, a "tapered-wave" incident field is used to avoid edge-scattering effects. A control parameter g determines the taper size of the incident field, and is set to $g = L/5$ for the image results of this paper. The tapered wave used in the numerical model is described in [5]. For the analytical solutions presented in the following section, the scattered field for the tapered incident beam can be obtained from a superposition of plane-wave responses with Gaussian weighting in the spectral domain. That is,

$$\Psi_s(k_{ix}, k_{sx}) = \frac{g}{2\sqrt{\pi}} \int_{-\infty}^{\infty} \psi_s(k_{ix} + k_x, k_{sx}) e^{-(k_x g/2)^2}\, dk_x \quad (2)$$

where ψ_s is the scattered field of a uniform plane-wave excitation, and k_{ix} and k_{sx} denote the wavenumbers of incident and scattered fields in the x-direction, respectively. The criteria presented in [6] show that the tapered wave chosen should provide accurate scattering results for incident angles up to 80°.

A numerical solution based on an iterative method of moments, called the forward–backward (FB) method, is used as a reference backscatter result. To improve the efficiency of the 1-D FB computation, the novel spectral acceleration (NSA) algorithm is employed [7]. The approximate theories applied include the local and nonlocal small-slope approximations (SSA/NLSSA) [2, 8–10]. The small-slope approximation (SSA), proposed by Voronovich, is based on a series expansion in generalized surface slope [2, 8]. SSA results have shown good agreement with exact solutions when moderate incident angles are considered (less than 45°), and when rms slopes of surfaces are relatively small (less than 30°) so that only a few series terms are required [9]. The nonlocal SSA (NLSSA) is an improvement of the SSA which attempts to include nonlocal interactions more accurately [10].

A 2-D SAR image of a deterministic surface can be constructed from a set of frequency and angular swept complex backscatter field data. Tomographic processing using an inverse Fourier transform with back projection is employed to generate the images of this paper [11]. To resolve surface variations on the order of a wavelength, backscatter data were collected over a 4 GHz frequency bandwidth (10–14 GHz) and a 20° angular bandwidth corresponding to 3.75 cm down- and 3.65 cm cross-range resolution in the image domain, respectively. Step sizes of 25 MHz and 0.2° are chosen so that image formation with large down-range (3 m) and cross-range unambiguous regions (7.2 m at $f_0 = 12$ GHz) are possible. A total of 16,000 backscattering calculations are required for image formation; the total image computing times on a 500 MHz processor varied from 135 h for the numerical model (reduced to 34 h by performing calculations in parallel on four computers) to 9 h for the SSA calculations.

Since image formation is closely related to the Fourier transform, there is a tradeoff between sidelobe level and spatial resolution. Window functions in both frequency and angle are chosen to set the relationship between these quantities. In this paper, the Hamming window is used to provide high resolution with moderate sidelobe levels [12].

3. 2-D BACKSCATTER RADAR IMAGES

Figure 2 illustrates *HH* and *VV* polarized radar images obtained from numerical backscatter results, in which the incident field approaches from the $-x$- and $+z$-directions. The surface profile is overlaid to allow determination of the effect of individual surface points, and the strongest scattering returns are observed near the center of the profile due to the tapered illumination applied. Significant polarization differences are observed in the figure, unlike the normal incidence case in which polarization differences were almost negligible [3]. The maximum levels of *HH* and *VV* images are -44.3 and -30.1 dB, respectively, showing a 14.2 dB difference. Another important difference between polarizations is the scattering source distribution over the surface profile. To observe these differences more clearly, images are plotted in Figure 3 over a 30 dB dynamic range for 2 m × 1 m portions of the original images. The images show single-scattering returns for *HH* backscatter to originate primarily from surface points with positive slopes (i.e., oriented toward the radar), while only small contributions are observed from points with negative slopes. *VV* returns, however, show scattering sources to be more evenly distributed over the surface, even including some contributions from the negative slope regions. These phenomena have previously been observed in [13], where examination of induced current distributions and local radar cross sections revealed similar results. Polarization dependence in rough-surface shadowed regions has also been discussed by Barrick [14]. The results are also consistent with a "composite" model since long-wave tilting effects are observed to be more significant in *HH* than in *VV* polarization. The general success of a two-term SSA theory (described below) also indicates that composite model ideas are appropriate for this case since the two-term SSA reduces to a composite theory in appropriate limits.

In addition to the strong single-scattering returns which appear on the surface profile in Figure 2, some multiple

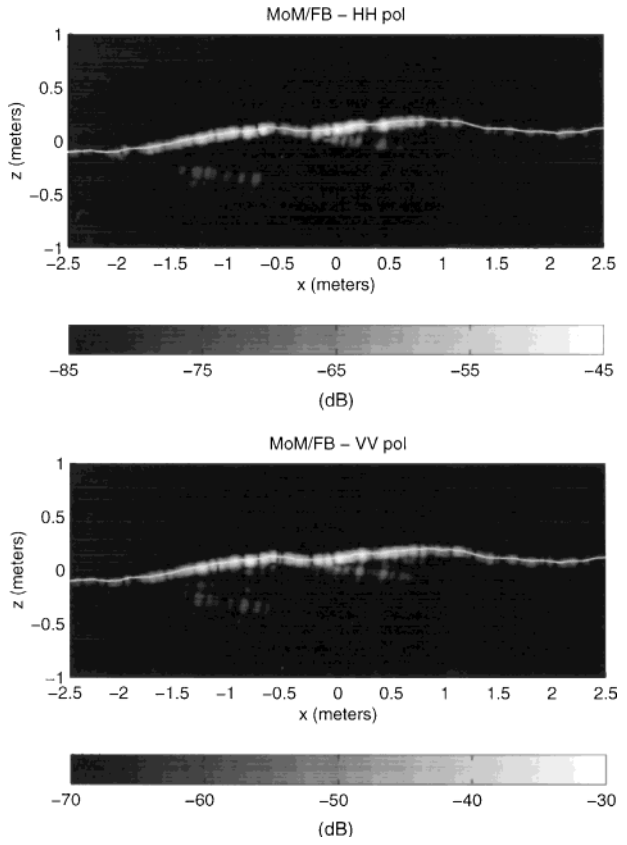

Figure 2 2-D ISAR images for an ocean-like surface at high incident angles ($w = 6$ m/s, $k_{dl} = 0.001$, and $k_{du} = 587$): MoM/FB, $f = 10$–14 GHz, $\delta f = 25$ MHz, $\theta_i = 60°$–$80°$, and $\delta\theta = 0.2°$

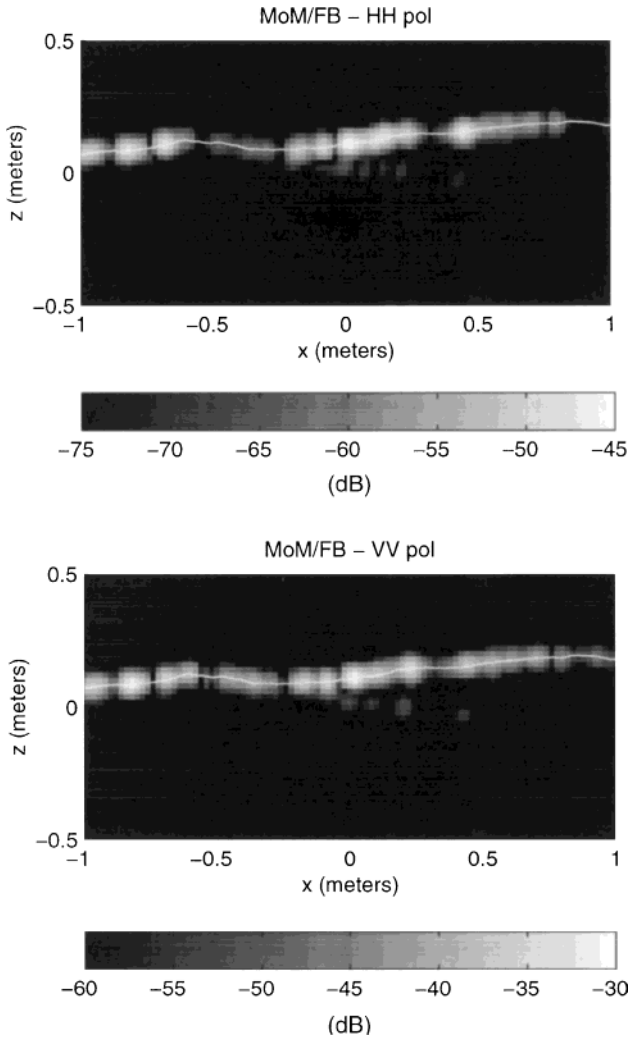

Figure 3 2-D ISAR images for an ocean-like surface: formed in a 2 m × 1 m range with 30 dB dynamic range

interaction effects are observed below the surface for both polarizations. In the Gaussian roughness cases at moderate incident angles, the level of multiple-scattering events was very low compared to the single-scattering events because the possibility of double-scattering events was greatly reduced as the incident angle increases [3]. This is not the case for P–M type rough surfaces due to the strong Bragg scatter effect which produces diffracted fields propagating outside the specular direction of a local "facet." By filtering the spectral content of the surface, the origin of both single and multiple interaction effects can be analyzed. Tests changing surface high and low cutoff frequencies showed Bragg scatter components to be the dominant source of single scattering, while multiple interaction events were related to the presence of both Bragg and large-scale surface components.

Images generated using the first two terms of the SSA are illustrated in Figure 4. Maximum image levels are -45.3 dB for *HH* polarization and -29.5 dB for *VV* polarization, both within 1 dB of numerical results. Some multiple-scattering effects are also observed, especially in the *VV* case, which were not captured by the SSA in studies with Gaussian spectrum surfaces [3]. Apparently, scattering interactions between Bragg and long-wave surface components are successfully captured by the two-term SSA. *HH* results, however, still underestimate the multiple interaction effects observed in the numerical solution. Overall rms errors [3] between numerical results and the two-term SSA are 0.7 and 1.1% for *HH* and *VV* pol, respectively. Images using only the first term of the SSA (not shown) obtain maximum levels of -50.1 dB for *HH* and -31.3 dB for *VV*, showing the underestimation of *HH* results observed previously in single-term SSA studies with ocean-like surfaces. Single-term SSA images also fail to illustrate any multiple interaction effects.

Radar images from the lowest order NLSSA are illustrated in Figure 5. Maximum image levels are -45.5 dB for *HH* polarization and -29.5 dB for *VV* polarization, within 1.2 dB of numerical results. The NLSSA images successfully capture both single and multiple interaction effects, even in *HH* polarization. The levels of the multiple interaction sources, however, continue to underestimate numerical results. Source distributions for single scattering are similar to both the SSA and numerical predictions. Overall rms errors in image space are 0.8 and 1.3% for *HH* and *VV* pol, respectively, slightly larger than those obtained with the two-term SSA.

4. CONCLUSION

Radar images of a Pierson–Moskowitz surface at oblique incidence angles have been considered. Images centered at 70° incident angle show some multiple interaction effects, and overall backscattering levels and multiple interaction contributions were found to be closely related to the Bragg scattering component in conjunction with the long-wave portion of the surface. The two-term SSA and lowest order

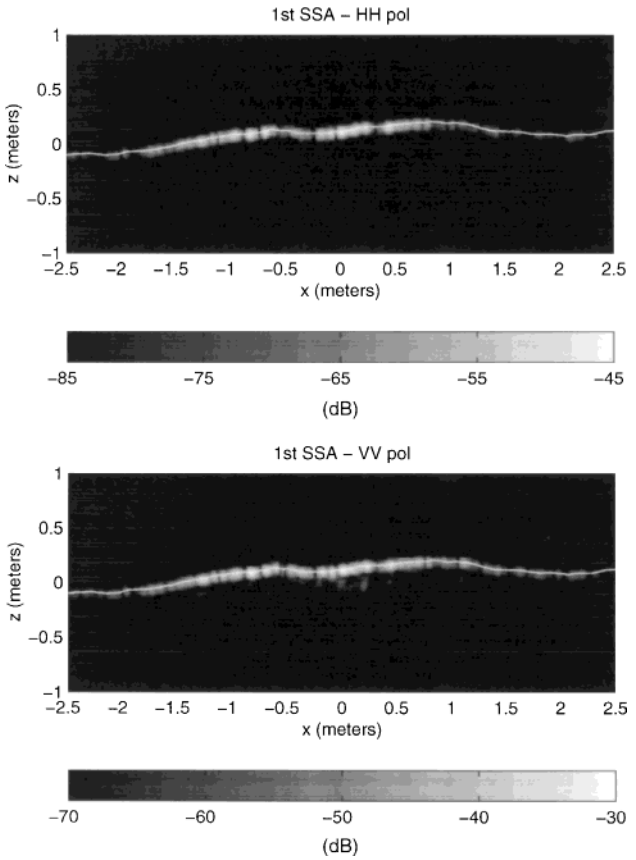

Figure 4 2-D ISAR images for an ocean-like surface at high incident angles ($w = 6$ m/s, $k_{dl} = 0.001$, and $k_{du} = 587$): first SSA, $f = 10$–14 GHz, $\delta f = 25$ MHz, $\theta_i = 60°$–$80°$, and $\delta\theta = 0.2°$

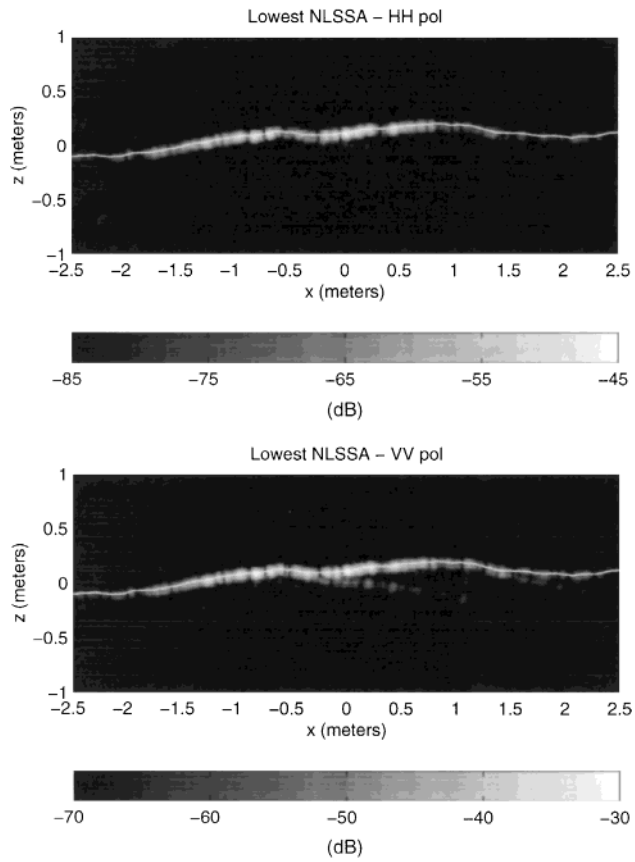

Figure 5 2-D ISAR images for an ocean-like surface at high incident angles ($w = 6$ m/s, $k_{dl} = 0.001$, and $k_{du} = 587$): NLSSA, $f = 10$–14 GHz, $\delta f = 25$ MHz, $\theta_i = 60°$–$80°$, and $\delta\theta = 0.2°$

NLSSA both predict single-scattering terms reliably, and capture some multiple interaction effects, but underpredict the level of multiple interaction terms. Images show strong polarization dependencies with approximately a 14 dB *VV/HH* polarization ratio, as well as polarization differences in the distribution of scattering sources over the surface profile. The studies of this paper demonstrate that radar images provide a means for better understanding of rough-surface scattering problems.

REFERENCES

1. L. Tsang, J.A. Kong, and R.T. Shin, Theory of microwave remote sensing, Artech House, Norwood, MA, 1985.
2. A.G. Voronovich, Wave scattering from rough surfaces, Springer Series on Wave Phenomena 17, 1995.
3. H. Kim and J.T. Johnson, Radar images of rough surface scattering: Comparison of numerical and analytical models, IEEE Trans Antennas Propagat (accepted, 2001).
4. G.R. Valenzuela, Theories for the interaction of electromagnetic and oceanic waves: A review, Bound Layer Meteorol 13 (1978), 61–85.
5. E.I. Thorsos, The validity of the Kirchhoff approximation for rough surface scattering using a Gaussian roughness spectrum, J Acoust Soc Amer 83 (1988), 78–92.
6. D.A. Kapp, A new method to calculate wave scattering from rough surfaces at low grazing angles, Ph.D. dissertation, Virginia Polytechnic Institute and State University, 1995.
7. H.-T. Chou and J.T. Johnson, Formulation of forward-backward method using novel spectral acceleration for the modeling of scattering from impedance rough surfaces, IEEE Trans Geosci Remote Sensing 38 (2000), 605–607.
8. E.I. Thorsos and S.L. Broschat, An investigation of the small slope approximation for scattering from rough surfaces. Part I. Theory, J Acoust Soc Amer 97 (1995), 2082–2093.
9. S.L. Broschat and E.I. Thorsos, An investigation of the small slope approximation for scattering from rough surfaces. Part II. Numerical studies, J Acoust Soc Amer 101 (1997), 2615–2625.
10. A.G. Voronovich, Non-local small-slope approximation for wave scattering from rough surfaces, Waves Random Media 6 (1996), 151–167.
11. D.L. Mensa, High resolution radar cross section imaging, Artech House, Norwood, MA, 1991.
12. F.J. Harris, On the use of windows for harmonic analysis with the discrete Fourier transform, Proc IEEE 66 (1978), 51–83.
13. D.J. Donahue, H.-C. Ju, and D.R. Thompson, Polarization dependent radar backscatter calculations from cresting ocean waves, Proc URSI, Boulder, CO, 1999, p. 262.
14. D.E. Barrick, Near-grazing illumination and shadowing of rough surfaces, Radio Sci 30 (1995), 563–580.